3 Safety Research for Nuclear Reactors (NUSAFE): Transmutation – Liquid Metal Technology –

3.1 Materials and oxygen transport and control in heavy liquid metal cooled subcritical systems (MYRRHA)

Long-living high-level radioactive waste from existing nuclear power reactors should be transmuted in short-living radio nuclides using fast neutrons provided by a spallation target in an accelerator driven subcritical system or by a fast nuclear reactor. The objective is to reduce the final disposal time of high-level radioactive waste (plutonium, minor actinides) from some 10^6 years down to about 1000 years. Lead (Pb) and lead-bismuth (PbBi) are foreseen as spallation-target and coolant of such devices.

The aim of the institute's contribution is the development of a suitable corrosion protection especially for parts under high loads like fuel claddings or pump materials in contact with liquid Pb or PbBi. Pulsed large area electron beams (GESA) are used to modify the surface of steels such that they fulfill the requirements of their surrounding environment. Corrosion test stands for exposure of specimens under relevant conditions are developed and operated. Test facilities for combined loads like erosion and corrosion and fretting corrosion were developed, built and operated. Conditioning the Pb with regard to its oxygen concentration and the transport of oxygen in PbBi are additional aspects of the work.

All tasks are embedded in European and international projects and cooperations like e.g. ESNII+, MaTISSE and MYRTE.

The most relevant results obtained in the reporting period are briefly presented:

3.2 Erosion-tests of promising materials for liquid metal pumps (MATISSE)

In MATISSE so called MAXPHASE materials (ternary carbides) are explored for their use in Pb alloy cooled nuclear systems. One objective beside the production of new types of such materials including CERMETS is the testing of their stability against erosion-corrosion in the CORELLA facility. Three different MAXPHASE materials (Zr_3AlC_2, Zr_2AlC, $(Nb,Zr)_4AlC_3$ ground & milled) and 316L steel ground as reference were tested under following conditions: Temperature – 500 °C, duration - 1000 h, LBE with [O] ~ $1x10^{-8}$ mass%, v ~ 8 m/s (800 rpm) – highly turbulent flow. Surface profilometry using a white light interferometer before and after the test run in combination with SEM observation of cross sections were employed for inspection. All specimens were cleaned from sticking LBE prior to inspection. Both Zr based Maxphases were broken during the take out, the NbZr Maxphases stay intact (Fig. 3.2.1). From the 316L sample not all LBE could be removed, which indicates an at least starting corrosion attack. At the Zr-based Maxphases no LBE remained after cleaning. However the Zr_3AlC_2 looks somehow attacked. The edges look rounded and the roughness increased significantly (Fig. 3.2.2). The SEM cross section of the Zr_3AlC_2 specimen reveals the formation of a Zr-oxide scale. The other Maxphases do not show any corrosion attack, which is in contrary to the 316L specimens considered as reference. There, the SEM cross section clearly shows a localized corrosion-erosion attack.

Fig. 3.2.1: Photos of specimens before and after 1000h erosion corrosion test at 500°C.

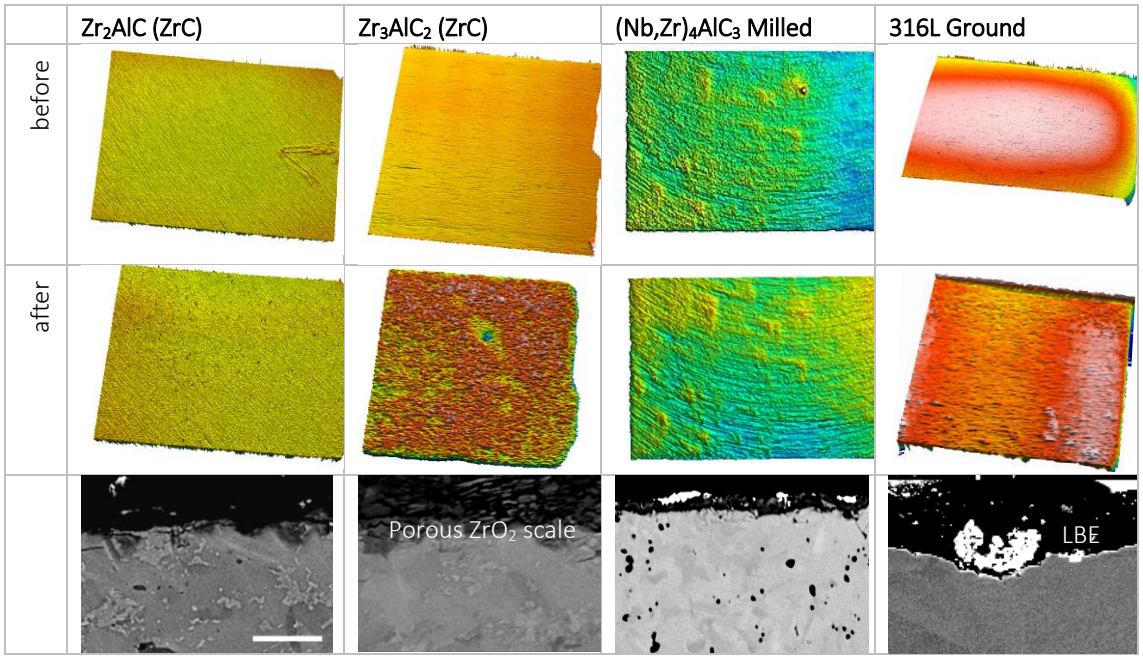

Fig. 3.2.2: Surface profiles and SEM cross sections of Maxphases before and after 1000h erosion corrosion test at 300°C.

3.3 Fretting tests in PbBi – wire wrapped configuration (MYRTE)

The MYRRHA reactor designed at SCK-CEN has a wire wrapped core configuration. The FRETHME facility used for fretting tests in liquid Pb-alloys in the past was designed for spacer grid fuel cladding configuration. Therefore, the sample holder were adapted to wire wrapped geometry allowing three geometrical configurations (parallel, cross and diagonal) having different contact areas. The contact pressure in cross configuration is about 10 times higher compared to the parallel arrangement (Fig. 3.3.1).

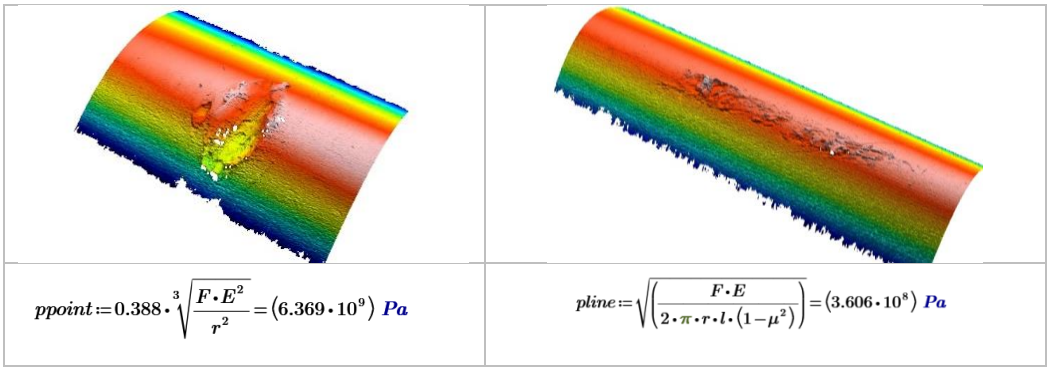

Fig. 3.3.1: Contact pressure of fretted samples in cross (left) and parallel (right) configuration.

To evaluate the influence of load, amplitude, time and geometrical configuration a set of experiments was performed during the internship of Mr. Nakabo from Japan. The load was varied between 20 and 100 N, the amplitude between 35 and 275 µm and the time from 100 to 300 h in cross and parallel and diagonal configuration (not all parameters are tested in all three configurations). All tests were performed with a frequency of 10 Hz in 400 °C hot PbBi having 10^{-7} wt% oxygen. The tested specimens were cleaned after the tests from residual PbBi and evaluated applying optical microscopy, scanning electron microscopy for surface and cross section inspection and white light interferometry for surface profilometry. Some experimental issues emerge during the tests; setting up the load especially at low values is quite challenging; the error resulting from this is significant larger at low loads compared to high loads; the parallel set-up is significantly more sensitive to misalignment compared to the cross configuration. Therefore, at time no final conclusions can be made, only preliminary tendencies are reported.

Varying in cross configuration the applied load at a constant amplitude range between 30 and 50 µm the maximum fretting depth increases first up to a turning point at a load between 50 N and 75 N and then decreases at 100 N load (Fig. 3.3.2 left). At higher amplitude of 150 µm the measured fretting depth of the 20 N test was disregarded due to experimental uncertainties. The two reliable fretting depths obtained at loads of 50 and 100 N indicate the excepted shift of the turning point to higher values at larger amplitudes.

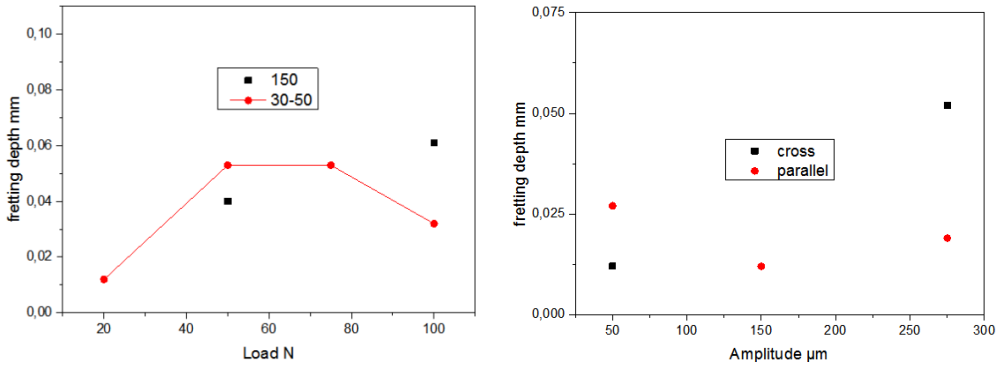

Fig. 3.3.2: (left) Maximum fretting depth as a function of applied load at constant amplitude of 30-50 µm and 150 µm (right) Maximum fretting depth as a function of amplitude at constant applied load of 20 N.

This phenomena is attributed to a threshold pressure required for the debris retention in the fretting area. Up to this threshold pressure the fretting depth increases as expected with increasing load. Further increase of load results in the retention and compaction of the debris and the creation of a kind of protecting layer. Comparing the fretting depth obtained with 20 N at different amplitudes in cross and parallel configuration two conclusions can be drawn (Fig. 3.3.2 right). First the difference in contact pressure between cross and parallel configuration is reflected in the difference in fretting depth. A more

detailed and perhaps quantitative analysis requires more experimental data that will be obtained in upcoming experiments. Second increasing the amplitude at constant load results in general in an increased fretting depth. Two SEM cross section (Fig. 3.3.3) made at the fretting area of the 20 N and 75 N specimen show the difference in damaging. At 20 N (Fig. 3.3.3 left) a kind of loose compacted debris is visible in the damaged area, the adjacent bulk material looks unchanged. At the 75 N specimen (Fig. 3.3.3 right) however, the debris is highly compact and the microstructure of the adjacent bulk looks deformed.

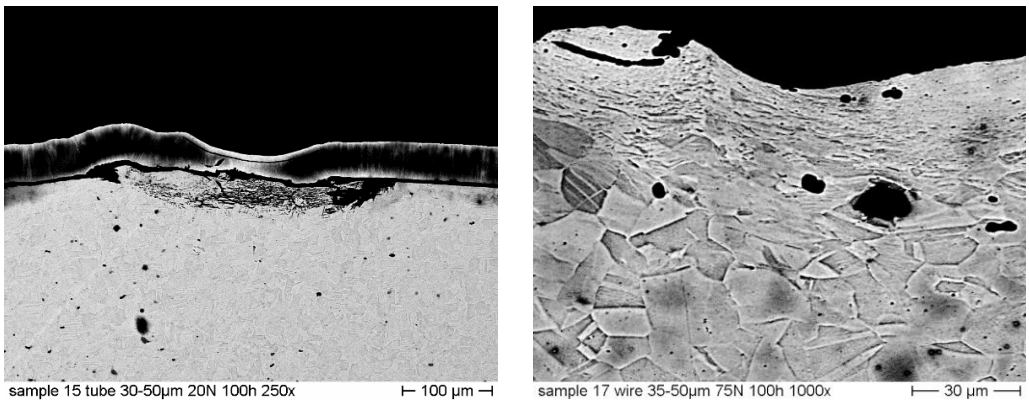

Fig. 3.3.3: SEM of cross section of tube tested with a 30-50 µm amplitude; left at load of 20 N; right at load of 75 N.

A reconditioning, including the exchange of some of the bearings, of the FRETHME facility to allow a more precise and reliable control of the amplitude is underway. After this dedicated experiments at 50 N, 100 h duration varying the amplitude between 25 and 200 µm to investigate the influence of the amplitude in more detail are targeted. In a second test cycle the duration will be changed from 100 h to 1000 h with a load of 50 N and a constant amplitude of 50 µm. Proceeding post investigations including the evaluation of the specific wear coefficient and possibly the prediction of expected wear at operating conditions are further objectives of this research.

3.4 Characterization of ODS under safety-related operation conditions (MaTISSE)

ODS (Oxide Dispersion Strengthened) alloy versions of ferritic steel can be a solution for high dpa resistant materials to be deployed in future GenIV nuclear reactors. Within the EU Horizon 2020 project MaTISSE, 9 and 12Cr-ODS are under investigation as potential fuel cladding materials. One focus is on their behavior in liquid lead under transient conditions and off-normal conditions like high temperatures as well as under low oxygen conditions. A test plan was established considering the analyses of representative DEC events of the ETDR (Alfred - EU project LEADER). In the conducted transient test the temperature of 550 °C was hold for 2000 h, increased to 750°C for 24h and hold again at 550 °C up to a total exposure time of 5000 h. Furthermore for comparison, tests with a constant temperature of 550 °C and 650 °C were conducted. For all tests an oxygen content of 10^{-6} wt% in the liquid lead was chosen. The ODS specimens were exposed in two conditions; as received or with a pulsed electron beam surface treatment. The latter was applied to homogenize the surface aiming to reduce localized corrosion. After GESA treatment 9Cr-ODS shows an around 23.5 µm restructured layer, while that of 12Cr-ODS was melted up to a depth of around 21 µm. However, the restructuring and cleaning was less prominent than expected.

The non-surface treated 9Cr-ODS sample showed after the transient test the known multilayer oxide on the surface consisting of magnetite, spinel and inner diffusion zone (IOZ) while the 12Cr-ODS sample showed a Fe rich Fe-Cr spinel with a IOZ underneath and at the border to bulk a Cr rich Fe-Cr spinel with Kirkendall Pores below. A negative influence of the temperature excursion was no detectable so far. At 650 °C (constant) after 2000 h a Cr-Mn-Si spinel with oxide roots was formed on the surface of 9Cr ODS. The roots show Pb inclusions and in one area dissolution attack was observed. After 5000 °C the entire surface showed a mixture between Cr-Mn-Si spinel with prominent Pb inclusions. Due to the higher Cr content the 12Cr ODS sample showed a slightly better corrosion behavior at 650 °C. A Cr-Mn spinel layer was formed at the surface with oxide nodes after 2000 °C and occasionally Pb inclusions can be observed after 5000 h exposure (Fig. 3.4.1). The changed microstructure in the GESA modified layer seems to favor diffusion along the grain boundaries, leading to an enhanced corrosion attack in time (Fig. 3.4.2). Exposure tests performed with the same material by CIEMAT (Madrid) at 600 and 700 °C in lead with 10^{-6} wt% oxygen showed a slightly improved compatibility of the GESA treated specimens compared with the non-treated ones.

Therefore, also considering the relatively weak changes in the microstructure of the treated area, the GESA parameters were investigated and adjusted to achieve an optimized structure. In addition an Al-coating applied by PVD was alloyed into the surface of the ODS samples using a GESA pulse. Such specimens are still exposed to Pb and the results will be reported as they are available.

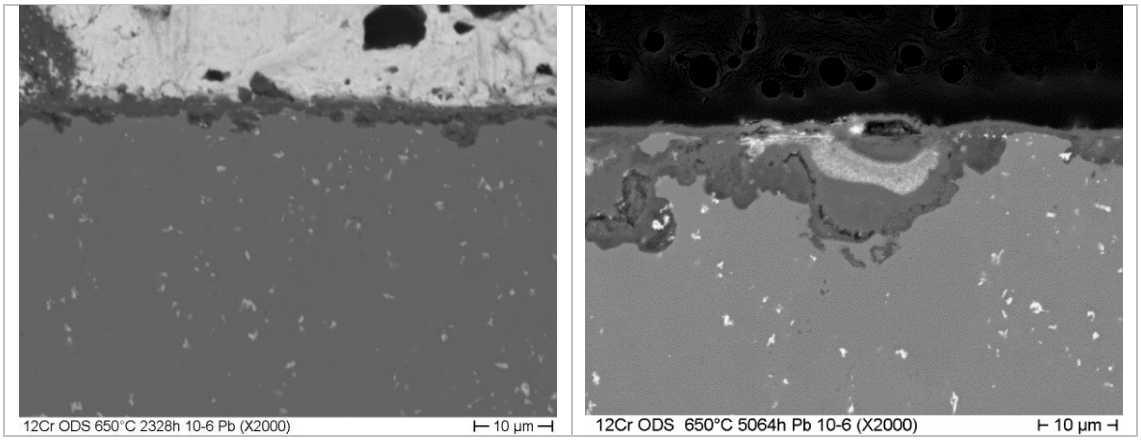

Fig. 3.4.1: SEM of 12Cr-ODS after exposure to Pb at 650 °C: left-after 2000 h, right after 5000 h.

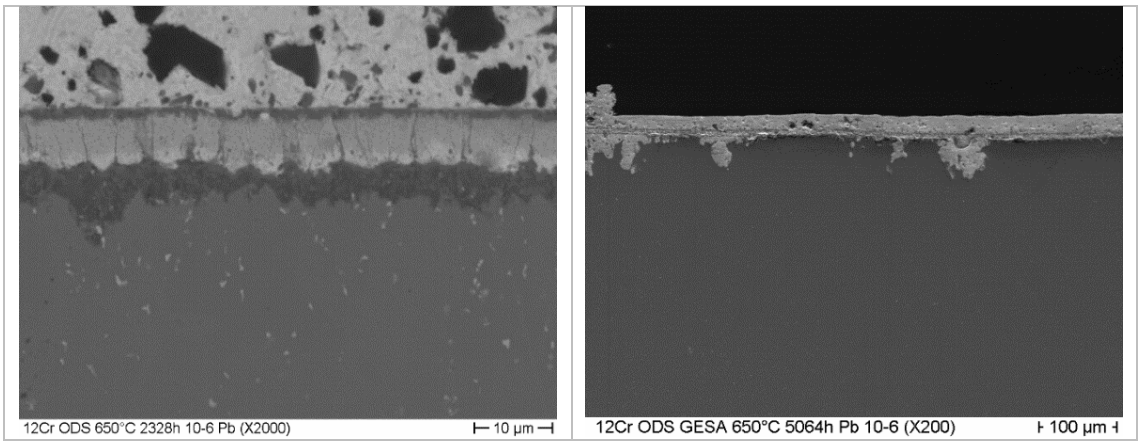

Fig. 3.4.2: SEM of 12Cr-ODS with GESA – pulse after exposure to Pb at 650 °C: left-after 2000 h, right after 5000 h.

3.5 Development of a Semiconductor-based Marx Generator for the GESA 1 device

The pulse power source currently driving the GESA 1 device consists of a LC-chain Marx generator using spark-gap switches and is capable of delivering a rectangular voltage pulse of around 120 kV to the cathode. As can be seen in Fig. 3.5.1 (left), the control grid is connected to ground via the resistor R_g causing a shift in the grid potential towards the cathode potential for increasing grid current. This negative feedback has a stabilizing impact on the cathode current. Due to the inherent dynamics of the cathode plasma, this passive control of the grid voltage via the grid resistor is insufficient in certain parameter ranges.

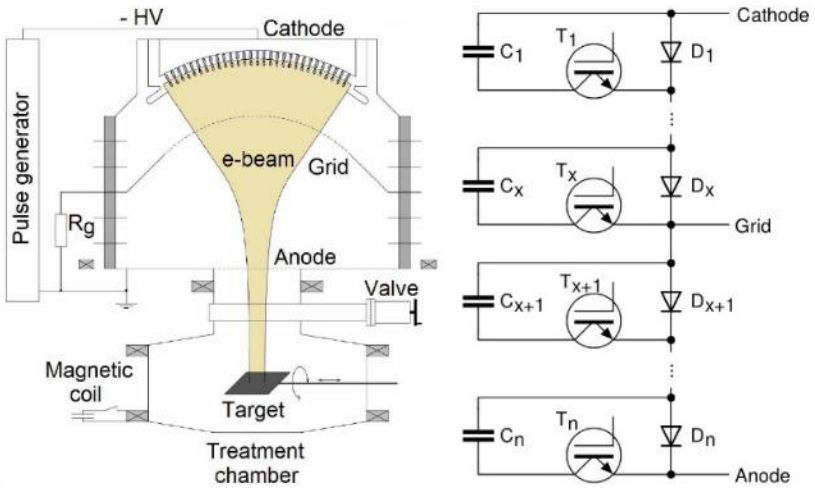

Fig. 3.5.1: Topology of the semiconductor-based Marx generator under development. Left: Schematic of the GESA 1 device, Right: Circuit.

The new pulsed power source currently under development will allow for a precise control of pulse length, cathode and grid voltage. The circuit topology is shown in Fig. 3.4.2 (right). The generator concept consists of around 150 individual modules, each comprising a capacitor (C), a switching element T and a by-pass diode (D). After all capacitors have been charged in parallel, closing the switching elements results in a series connection of the capacitors and, hence, a voltage multiplication at the output. Due to the by-pass diodes, stages may remain inactive, not contributing to the output voltage pulse. By subsequently opening or closing the switches during the pulse, the output voltage can be modified according the number of active stages and the remaining charge in their capacitances. For a direct control over the grid voltage, the grid is planned to be connected directly to the generator as can be seen in Fig. 3.4.2 (right), thereby allowing for a nearly independent control of grid and cathode voltage.

The main challenge for the employed switching elements is the required fast voltage rise time for a homogeneous cathode plasma ignition of around 100 kV/100 ns. This necessitated the development of a gate-boosting circuit for the IGBT switches as well as a fast optical signal transmission for trigger signal distribution. On each stage, a fast microprocessor and logic circuitry handle the switching signal generation during the pulse to create desired output voltage shape. The capacitor voltage droop during the pulse is compensated by subsequently adding active stages once the output voltage has dropped by 1 kV. Thereby, a flat top quality is expected to be around 1 %. The resulting high number of stages will be addressed via optical communication from a control unit handling the fast signal distribution, whereas the user interface for designing the output voltage shape will be situated on a PC. In the current stage of the project, the first stage of the Marx generator has been operated successfully in the complete control chain consisting of a preliminary PC user interface, the control unit and the stage itself. The graphs in Fig. 3.5.1 show first results

for one stage with the final output capacitance of 200 µF with 6 IGBTs in parallel configuration. The upper graph of Fig. 3.5.1 thereby shows the load current (red trace) of 250 A with a rise time of around 50 ns together with the voltage across the switching elements. The lower graph shows an example of the feasible arbitrary waveform generation. After the verification of the generator concept in a small scale version, the complete generator is scheduled to be operational in fall 2017.

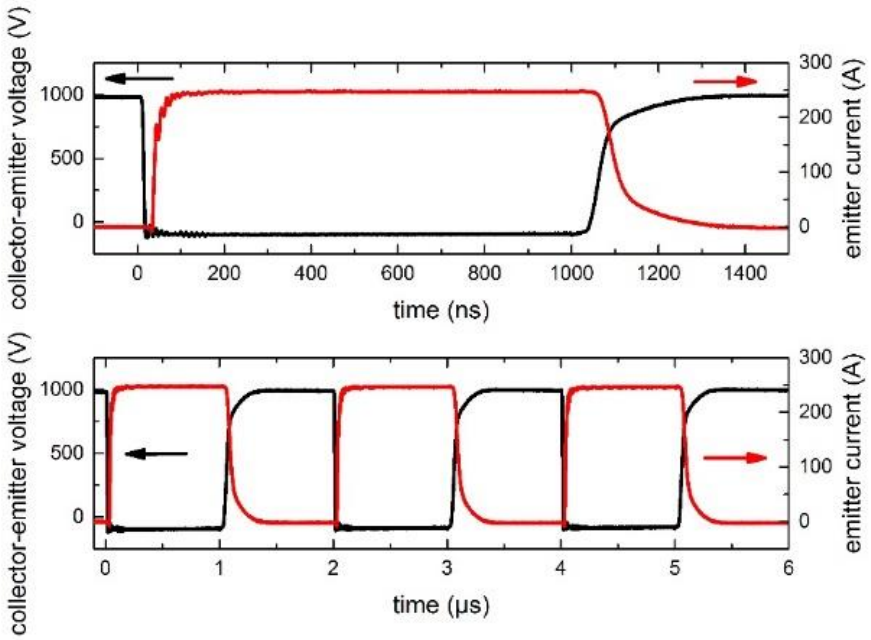

Fig. 3.1.8: Output voltage and current waveforms for one pulse (upper graph) and for an arbitrary waveform (lower graph).

3.6 GESA Beam Dynamics Simulations

The cylindrical triode-type pulsed electron accelerator GESA IV was specifically designed for surface treatment of cylindrical tubes such as cladding tubes of GEN IV fission reactors. However, due to the large difference between cathode and grid diameter on the one hand and the comparatively small target (anode) diameter on the other hand, unstable operation and inhomogeneous treatment is often observed. This may be caused by the formation of a virtual cathode between grid and anode or by the large distortion of electron trajectories due to the self-induced magnetic field. Another crucial phenomenon is the generation of ions at the target. In order to understand the underlying processes and improve the beam homogeneity and stability, a systematic numerical study of GESA IV beam performance was undertaken in the reporting period. Stable and homogeneous operation regimes could be identified.

For the numerical study, the PIC code simulation package MAGIC2D by Orbital ATK, USA, was used. The system geometry is shown below. A high voltage pulse is applied to the cathode via the input port. The potentials of cathode and grid against the grounded anode are controlled via the resistors R_{cg} and R_{ga}. Beam current reaching the target flows in axial direction along the target to the outer boundary. Primary beam electrons are generated at the cathode via the explosive emission routine. The beam electrons then move in accordance with the relativistic Lorentz equation in the free space of the simulation area until they hit a conductor. Backscattering of electrons at the target is included, i.e., when electrons hit the surface, secondary electrons (backscattered electrons) are emitted according to the target material specifications (in the shown case aluminum). The third type of charged particles considered in the simulation are protons. If included, they are emitted from the target surface obeying the space charge limit. Once emitted, also ions move according to the Lorentz equation until they hit a conductor.

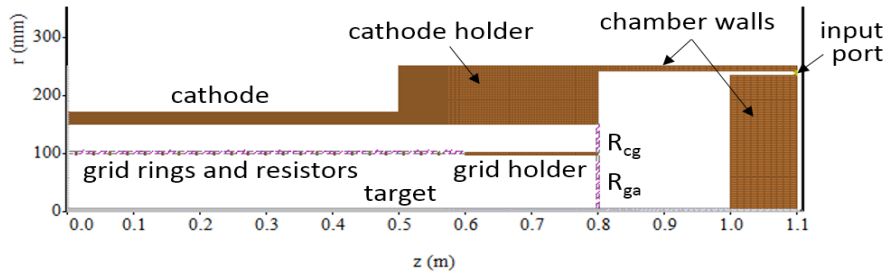

Fig. 3.6.1: System geometry. Mirror symmetry at z=0 is assumed as well as azimuthal symmetry. The accelerator is composed of the outer chamber walls, cathode and cathode holder, grid rings and grid holder, and the target anode. Line resistors R_{cg} and R_{ga} connect cathode holder, grid holder, and target. Additional line resistors connect the individual grid rings.

First, unipolar electron flow is considered, i.e., protons are not included in the simulations. The performance of unipolar flow is of interest for the initial stage of pulsed electron beam application when ion generation at the target and ion motion towards the cathode are negligible. The cathode voltage is fixed at U_{ca} = 120 kV in the simulations, while the ratio of the controlling resistors R_{cg} and R_{ga} is varied. Results of the simulation with U_{cg} = 18 kV are shown in the figure.

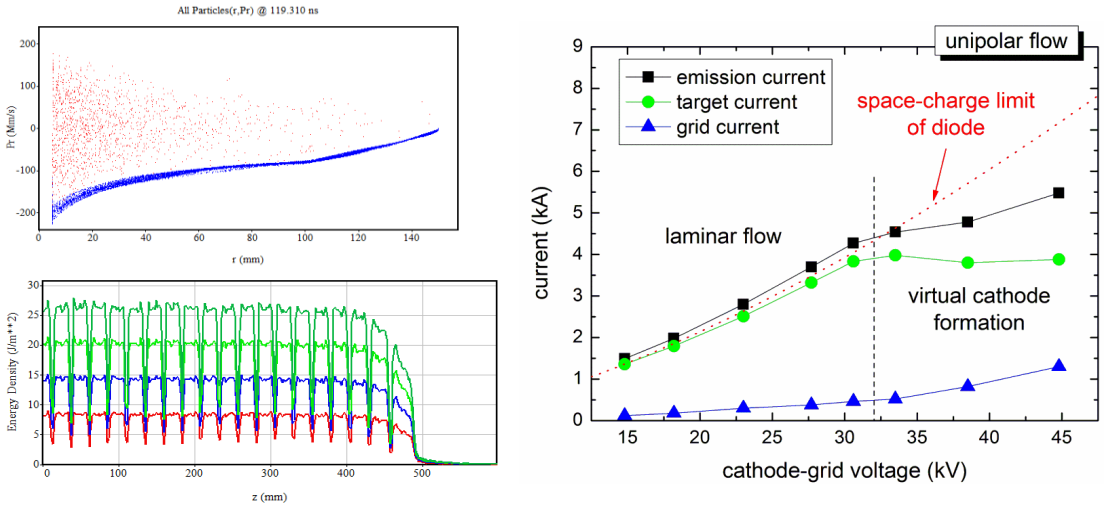

Fig. 3.6.2: Simulation results for unipolar flow and constant cathode-anode voltage 120 kV. Left: Situation for U_{cg} = 18 kV. (a) Radial momentum versus radial position; blue dots represent primary beam electrons, red dots indicate electrons backscattered at the target; (b) accumulated beam energy density at target surface versus axial position at four times between 47 ns and 119 ns. Right: Emission, target, and grid currents of the full length accelerator versus cathode-grid voltage.

The beam electrons (blue dots) are continuously accelerated from the cathode at r = 150 mm via the grid at r = 100 mm to the anode at r = 5 mm. The radial momentum of all beam electrons is negative, i.e., no primary electrons return towards the cathode. Backscattered electrons (red dots) are found mainly in the vicinity of the target. The beam energy density measured at the target is homogeneous (except the positions shaded by the grid rings). Laminar flow of beam electrons is obtained.

The emission current, grid current, and target current of the full accelerator are also shown in the figure for various grid potentials. Two different regimes are found, with the transition occurring at a cathode-grid voltage of about 32 kV. The previously described situation of laminar flow is obtained below this threshold. The emission current of the laminar flow regime agrees very well with the predicted space-charge limit of the corresponding cylindrical diode. Thus, processes between grid and target do not influence the beam characteristics in the cathode-grid gap.

For cathode-grid voltages above the laminar flow threshold of ~32 kV, the emission current stays well below the space charge limit of the corresponding diode. As the cathode-grid voltage is increased and the emission current and space charge become larger, a potential well between grid and target is formed and grows until a virtual cathode is obtained, see next figure. Due to electrons returning towards the cathode, the space charge also in the cathode-grid gap is increased, which lowers the emission current. Another consequence of the formation of a virtual cathode is the inhomogeneous beam power density at the target.

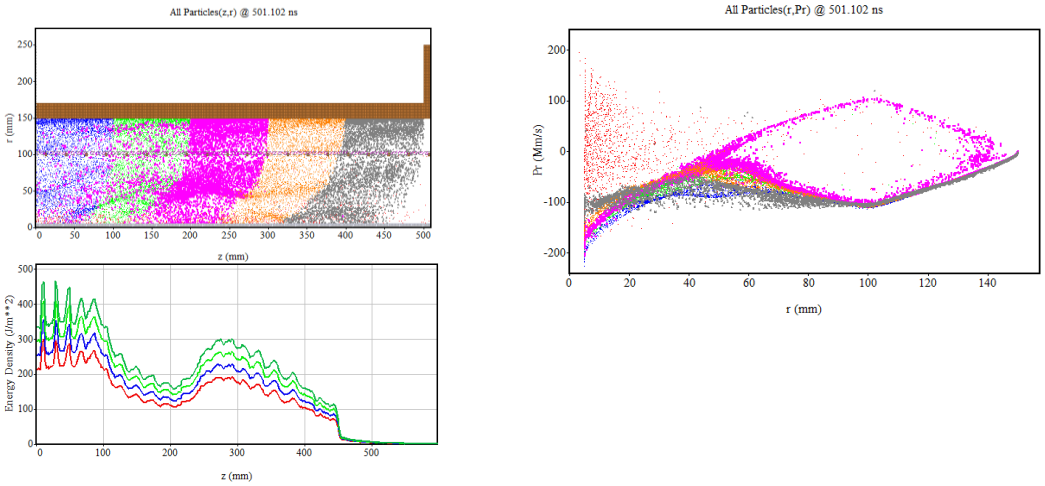

Fig. 3.6.3: Virtual cathode formation, observed for unipolar flow with U_{cg} = 33.5 kV: (a) particle distribution in (z,r) space, (b) radial momentum distribution versus radial position; beam electrons are represented by, respectively, blue, green, pink, orange, and grey dots; electrons backscattered at the target are represented by red dots; (c) accumulated beam energy density distribution at the target surface versus axial position at four times between 329 ns and 501 ns.

In order to achieve melting during target treatment, pulse durations in the microsecond range are usually chosen. On such time scales, ion flow from the target cannot be neglected. Therefore, space charge limited ion emission from the target is introduced in the simulations and the situation of bipolar flow is studied. The next figure shows the emission, target, and grid electron currents of bipolar flow for the full range of cathode-grid voltages investigated. Again a regime of laminar flow is found for low cathode-grid voltages. In this regime, the presence of counter-streaming ions results in an increase of the electron emission current by roughly 50 % against unipolar flow.

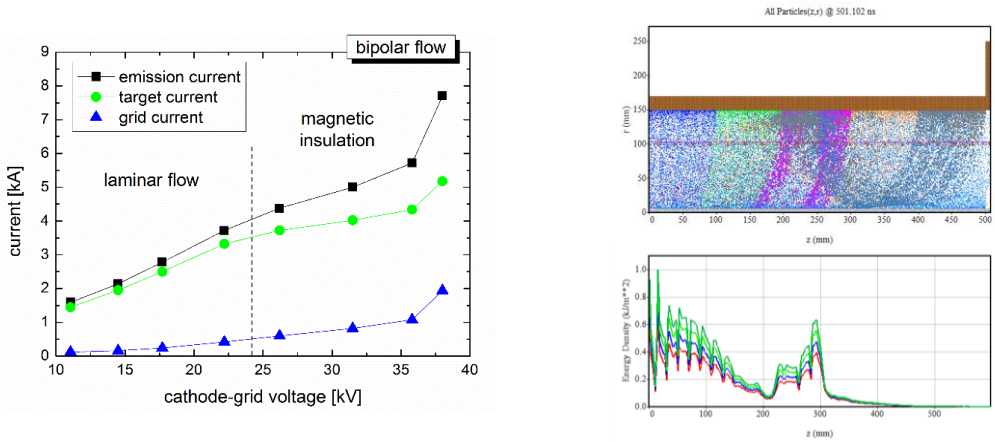

Fig. 3.6.4: Simulation results for bipolar flow and constant cathode-anode voltage 120 kV. Left: Emission, target, and grid currents versus cathode-grid voltage. Right: Situation for U_{cg} = 35.8 kV. (a) particle distribution in (z,r) space; beam electrons are represented by, respectively, blue, green, pink, orange, and grey dots; electrons backscattered at the target are represented by red dots, ions are represented by light blue dots; (b) accumulated beam energy density distribution at the target surface versus axial position at four times between 329 ns and 501 ns.

Beyond a cathode-grid voltage of ~24 kV the electron emission current seems to be reduced against the trend observed for laminar flow, although virtual cathode formation is not observed for bipolar flow. The reason for the emission reduction is magnetic insulation. The further away from the central axial position, the higher is the accumulated target current. The higher induced azimuthal magnetic field results in stronger bending of the electron trajectories on their way towards the target. Beyond a certain magnetic field strength, electrons are unable to reach the target and return towards the cathode (magnetic insulation). In the particular case shown in the figure, all electrons emitted at axial positions larger ~350 mm are unable to reach the target directly (i.e., all 'grey' electrons and some of the 'orange' electrons).

The increased electron space charge in the cathode region due to returning electrons from the beam edge leads to a reduced emission current. Returning electrons also result in an increase of the grid current and in an inhomogeneous beam power density at the target.

To summarize, simulations of the beam performance of the cylindrical pulsed electron beam accelerator GESA IV at given cathode voltage -120 kV showed different operation regimes depending on the cathode-grid voltage applied. For low cathode-grid voltages and low beam current, laminar flow conditions with homogeneous energy density at the target are obtained. The laminar flow regime exists for both unipolar electron beams and bipolar beams with counter-streaming ions generated at the target. It is the only feasible operation regime for homogeneous treatment of metal surfaces.

3.7 AFA-Alumina-forming austenitic – steels

Alumina-forming austenitic alloys, exhibiting high-temperature creep strength and oxidation resistance in dry and humid air, are a relatively new class of stainless steels. These main characteristics are due to the formation of stable nano-NbC, submicron B2-NiAl and Fe_2Nb Laves precipitates, which determine the creep resistance increase and the formation of an alumina protective scale, which improves the oxidation resistance in the 600-900 °C temperature range. The above mentioned properties, make alumina-forming austenitic steels potential candidates for structural materials in energy related applications.

So far only one attempt, performed by a research group from KTH – Stockholm, was made to evaluate the compatibility (at 550°C) of this class of stainless steels with heavy liquid metals, which are considered as working fluids in several energy-related applications. Therefore a systematic study is mandatory for defining the composition of alumina-forming stainless steels having compatibility with such environments.

Some preliminary results concerning the corrosion behaviour of alumina-forming austenitic steels, during their exposure to oxygen-containing molten lead, are reported below.

Two model alloys of FeCrAlNiX system (X: Ti, Nb, Zr, Mn), designed using Thermo-Calc software, to form protective alumina scale and in the same time to preserve the austenite structure during long term exposure in heavy liquid metals, were prepared by arc melting under argon atmosphere. XRD patterns of the as-cast alloys are presented in Fig. 3.7.1.

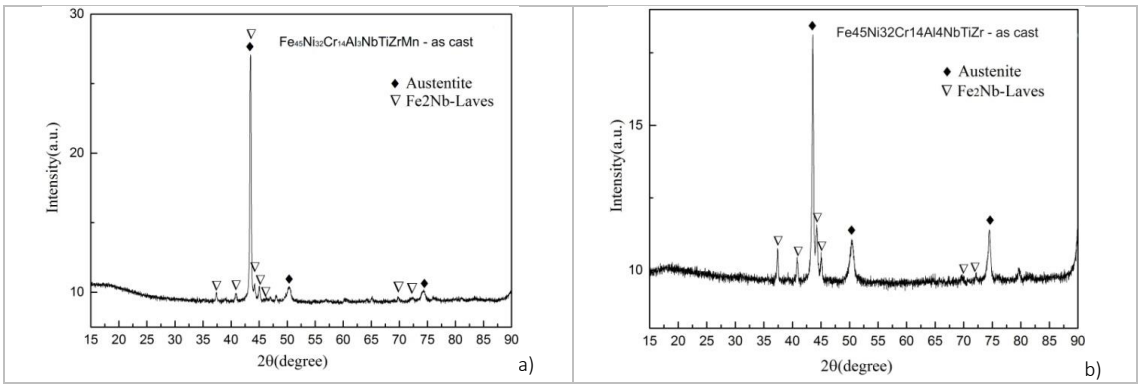

Fig. 3.7.1: XRD patterns of aluminium-containing stainless steels in as cast state: f.c.c. matrix and Fe2Nb Laves phase.

The constituting phases of both alloys are austenite (face centered cubic - f.c.c.), as matrix, and Fe_2Nb-type Laves phase (hexagonal) precipitated at the austenite grains boundaries.

The typical microstructure of the as-cast model alloys is presented in Fig. 3.7.2.

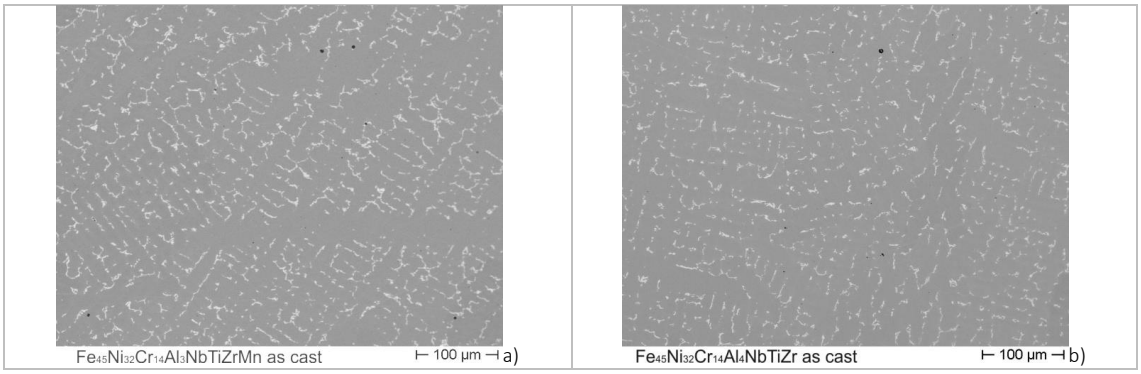

Fig. 3.7.2: SEM backscattered electron images of the model alloys in the as-cast state: f.c.c matrix with Fe_2Nb Laves phase at the grains boundaries.

Samples cut from these model alloys were exposed in stagnant molten lead with 10^{-6} wt.% oxygen, at 600°C for 2100 hours.

The morphology of the oxide scales grown, during the exposure to oxygen-containing liquid lead, on the surface of the specimens was examined by SEM. No dissolution attack was observed for any of the samples tested. The general aspect is generally smooth as can be observed in Fig. 3.7.3.

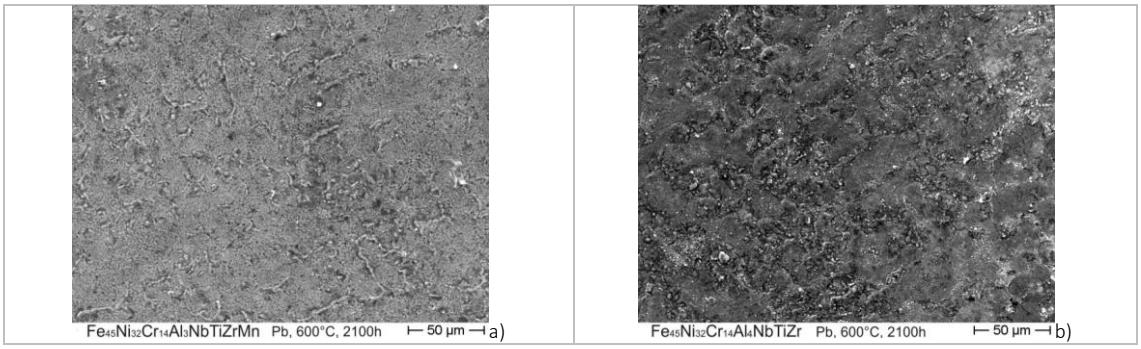

Fig. 3.7.3: The morphologies of the oxide scales grown during the exposure to oxygen containing liquid lead on the surface of the specimens.

The evaluation of the thickness and of the chemical compositions of the oxide scale, grown during exposure to oxygen-containing liquid lead, was performed on the cross sections of the exposed specimens. It was observed that the specimens were protected by a thin (300-400 nm) inward growing oxide scale, rich in Al and Ti, on around 80 % of their surface, while the remaining part were covered by islands of a thicker, also inward growing, Al-Cr-oxide (Fig. 3.7.4).

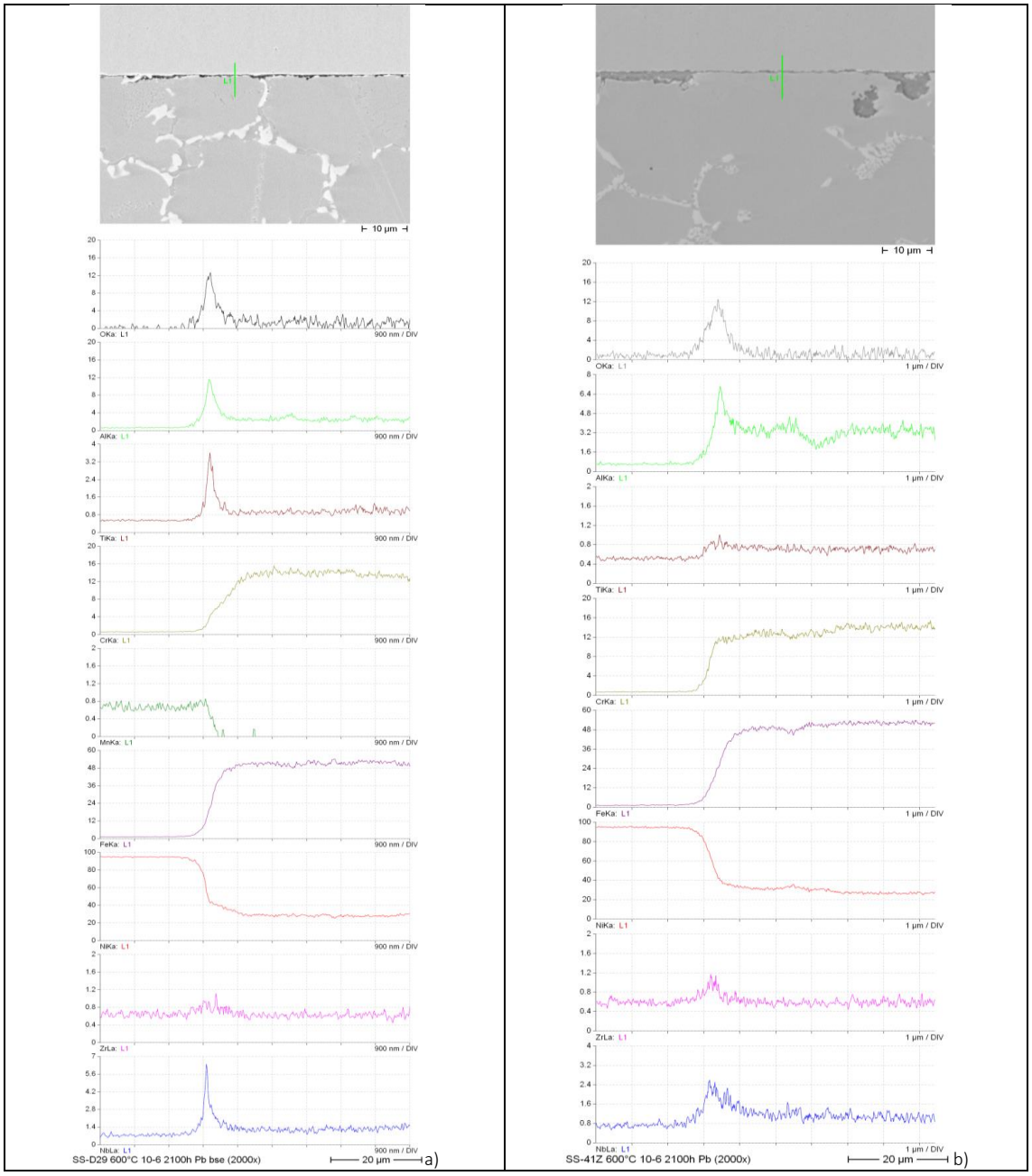

Fig. 3.7.4: EDX line scans of the thin oxide scale grown on the model alloys $Fe_{45}Ni_{32}Cr_{14}Al_3NbTiZrMn$ (a) and $Fe_{45}Ni_{32}Cr_{14}Al_4NbTiZr$ (b).

Involved Staff:

DP W. An, Dr. R. Fetzer, Y. Nakabo (Internship), A. Neukirch, Dr. A. Heinzel, DI. M. Hochberg, Dr. A. Jianu, DI (Fh) F. Lang, Prof. G. Müller, Dr. G. Schumacher (Gast), H. Shi (SCS-PhD student), W. Zhen (SCS-PhD student), A. Sivkovich, **Dr. A. Weisenburger**, DI (Fh) F. Zimmermann.